ACS APPLIED ENERGY MATERIALS

Article

High-Performance Titanium Oxynitride Thin Films for Electrocatalytic Water Oxidation

Nikhil Reddy Mucha, Jacob Som, Jonghyun Choi, Surabhi Shaji, Ram Krishan Gupta, Harry M. Meyer, Corson L. Cramer, Amy M Elliot, and Dhananjay Kumar

ACS Appl. Energy Mater., **Just Accepted Manuscript** • DOI: 10.1021/acsaem.0c00988 • Publication Date (Web): 04 Aug 2020

is published by the American Chemical Society. 1155 Sixteenth Street N.W., Washington, DC 20036

High-Performance Titanium Oxynitride Thin Films for Electrocatalytic Water Oxidation

Nikhil Reddy Mucha[1], Jacob Som[1], Jonghyun Choi[2], Surabhi Shaji[1], Ram K. Gupta[2], Harry M. Meyer[3], Corson L. Cramer[4], Amy M. Elliot[4], Dhananjay Kumar[1]*

[1]Department of Mechanical Engineering, North Carolina Agricultural and Technical State University, Greensboro, NC 27411

[2]Department of Chemistry, Pittsburg State University, Pittsburg, KS 66762

[3]Center for Nanophase Materials Sciences, Oak Ridge National Laboratory, Oakridge, TN 37831

[4]Energy and Transportation Sciences Division, Oak Ridge National Laboratory, Oakridge, TN 37831

Abstract

TiN_xO_y (TiNO) thin films with superior electrochemical properties have been synthesized in situ using a pulsed laser deposition method and a varied oxygen partial pressure from 5 to 25 mTorr. The electrochemical overpotential of these TiNO films for water oxidation was found to be as low as 290 mV at 10 mA/cm^2, which is amongst the lowest overpotential values reported. The Tafel slopes, indicative of a rate of increase of electrode potential with respect to current, for these films, are determined to be in the range of 85-57 mV/decade. These results further demonstrate the superiority of TiNO thin film as electrocatalyst for water oxidation to generate fossil-free fuels. The improvement in the electrocatalytic behavior of the semiconducting TiNO thin films is explained based on an adjustment in the valence band maximum edge and an enhancement in the number of electrochemically active sites. Both effects are realized by the substitution of N by O forming, TiNO lattice which, is isostructural with the rock-salt TiN lattice. These findings appear to assume significant importance in light of water electrolysis to produce fuels for the development of environmentally friendly power sources.

Keywords: oxynitrides, oxygen evolution reaction, electrocatalysis, electrochemical overpotential, water splitting, thin films, pulsed laser deposition

1. Introduction

The research efforts toward developing an easy-to-synthesize high conductivity anode electrocatalysts that are relatively inexpensive, stable, and active at low overpotentials during water splitting are challenging. The requirements for these developments are stringent and have often hindered the practical use of the precious metals such as Pt, Pd, Ru, Ir, etc. and oxides such as RuO_2, IrO_2 in the electrochemical systems. A large difference in the electronegativity values between titanium (Ti) and oxygen (O) as well as nitrogen (N) enables Ti to react easily with oxygen and nitrogen to form titanium dioxide (TiO_2) and titanium nitride (TiN). The simplicity in the synthesis and the embodiment of myriads of unique properties in TiN and TiO_2 place these two compounds among the most widely studied and used materials. After the work of Honda and Fujishima, TiO_2 has become a paradigm material in surface science and catalysis.[1-7] TiN exhibits an unusual combination of covalent, metallic, and ionic properties: ultra-hardness (close to that of the diamond), high thermal conductivity, high electrical conductivity (higher than that of Ti), and even low- temperature superconductivity.[8-16] Several Ti-based oxynitrides (TiN_xO_y, abbreviated as TiNO) compounds, intermediate between metallic TiN and insulating TiO_2, have gained enormous scientific and engineering attention recently due to progressive and favorable change in their properties opening the doors for many applications.[2, 3, 9, 17-22] Oxynitride stabilities in air and moisture are greater than those of the pure nitrides but have smaller bandgap than those of comparable oxides.[20, 22-29] There is no isostructural phase between TiN and TiO_2. However, TiN is isostructural with rock-salt $TiN_{0.5}O_{0.5}$ (obtained with 50 % substitution of N by O in TiN).[19, 30, 31] The rock-salt structure of TiN and $TiN_{0.5}O_{0.5}$ are shown in Figure 1. Due to a random substitution of N by O and a concomitant change in the valence state of Ti, and consequently, ionic radii, the lattice parameters (a, b and, c) along the x-, y-, and z-axis do not remain same. Accordingly, the three orthogonal angles (α, β, and γ) would also deviate from 90°. Thus, the oxidation of TiN is expected to shift to monoclinic crystal symmetry from cubic. However, the base rock-salt type

structure remains intact. Hence, it is favorable to oxidize TiN to TiNO as the incorporated O atoms are already in their most stable structure, namely, rock-salt. Moreover, in this way, the main drawback of an extra-electron transfer during N-incorporation in TiO_2 is overcome.[9, 30-32]

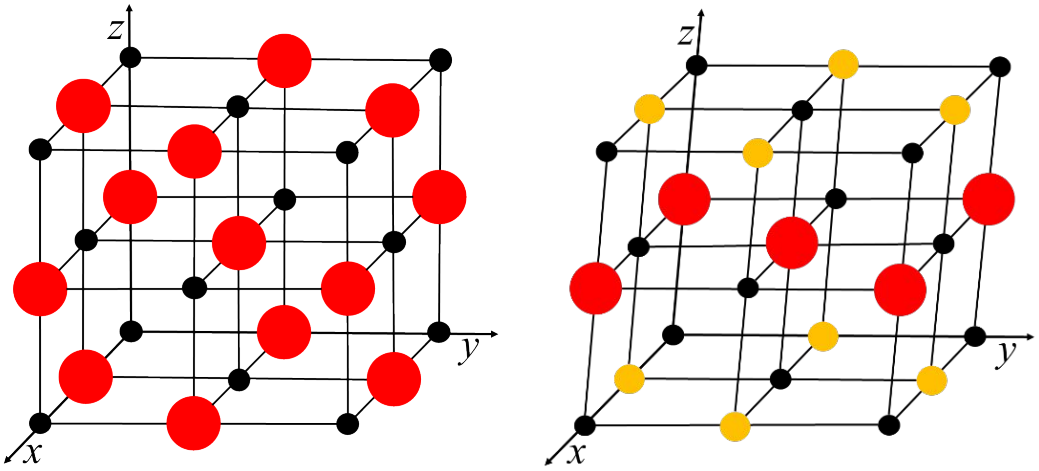

(a) (b)

Figure 1. Unit cell crystal structures of (a) TiN, (b) $TiN_{0.5}O_{0.5}$, Ti^{3+} ● = 0.081 nm, N^{3-} ● = 0.132 nm, and O^{2-} ● = 0.100 nm.

The present study has focused on the synthesis of TiN_xO_y thin films with varying x and y and the study of their performance in water splitting for oxygen evolution. The overpotentials for oxygen evolution reaction (OER; $4OH^- = O_2 + 2H_2O + 4e^-$)[33] realized for these films are in the range of 320 to 290 mV (at 10 mA/cm^2) which are amongst the lowest values reported for metal alloys, oxynitrides, and oxide systems, designed using extrinsic as well as intrinsic approaches.[3, 17, 27, 34] The materials design via the extrinsic approach is generally based on increasing the loading capacity of the electrocatalysts via defect engineering and/or surface modification, while the intrinsic approach is based on exploring novel materials with an enhanced electroactivity.[35-37] The improvement in the electrocatalytic behavior of TiNO thin films is explained based on the enhanced number of electrochemically active sites realized by the substitution of anionic N sites by O and a favorable alignment of valence band with respect

to the redox potential of electrolyte medium.[19, 27] These findings are of significant importance in light of water electrolysis to produce fossil-free fuels for the development of environmentally friendly power sources.[35, 38] Although there are some reports on the electrocatalytic activity of TiNO system, the majority of the reports are focused on TiNO system in the polycrystalline bulk form.[3, 39-42] The significance of TiNO thin film research arises from better possibilities in precisely controlling the orientation, crystallinity, composition, grain size, and grain distribution, which are well known to critically affect the film's properties.[9, 18, 19, 43-45] The TiNO material system in thin film form has also a strong potential for integration with technologically important substrates such as silicon and sapphire due to the small mismatch in lattice constants and thermal expansion coefficients.[46, 47]

2. Experimental Section

TiNO films were deposited on single crystal c-plane sapphire (0001 orientation) substrates using a pulsed laser deposition (PLD) method. A high purity (99.99%) titanium nitride composite target was used to deposit TiNO films by controlling the oxygen pressure, substrate temperature, laser energy density, laser repetition rate, etc. An excimer laser (Coherent Complex Pro) with krypton fluoride (KrF) radiation (wavelength 248 nm, pulse duration 30 ns) was used during the PLD experiments. The frequency of the laser beam was 10 Hz. A fixed number of laser pulses (shots) of 20,000 (deposition time = 2,000 s) was used. Some other parameters specific to our PLD experiments include substrate temperatures of 400 °C, oxygen pressure in the range of 5 to 25 m Torr, the laser energy density of 2 J/cm^2. The details of our PLD set-up are described elsewhere.[9, 10, 48-50] The crystallographic studies and phase purity of TiNO films were carried out using Bruker D8 advanced X-ray diffractometer. X-ray photoelectron spectroscopy (XPS) was performed using a Thermo Scientific (Waltham, MA, USA) Model k alpha XPS instrument. Survey spectra were acquired for qualitative and quantitative analysis. High-resolution core level spectra were acquired for detailed chemical

state analysis. The surface morphology of TiNO films was studied using Hitachi SU8000 scanning electron microscopy (SEM).

The electrical resistance of TiNO films was measured using a Quantum Design Physical Property Measurement System. The electrical resistivity (ρ) was determined using a standard four-probe measurement which eliminates the contributions from the contact resistance The expression used in the calculation is: $\rho = \left(\frac{V}{I}\right)\left(\frac{w.t}{l}\right)$, where V is the voltage developed across two intermediate voltage probes, I is the current applied through the two extreme probes, w is the width of the sample, t is the thickness of the sample, and l is the distance between the two voltage probes. Thin gold wires (~0.1 mm diameter) were attached to four circular indium pads placed on the top surface of TiNO films. In this method, no conductive layer is needed from the bottom side of the TiNO films. In the calculation of ρ, the exact dimensions (l×w) of TiNO samples were used which were measured to be 6.09 mm × 5.16 mm, 5.99 mm × 6.08 mm, 6.12 mm × 5.86 mm, 6.03 mm × 5.88 mm for samples deposited under 5 mTorr, 10 mTorr, 15mTorr, and 25 mTorr of oxygen, respectively.

The electrochemical activities of TiNO samples were analyzed using linear sweep voltammetry (LSV), cyclic voltammetry, and electrochemical impedance spectroscopy. The electrochemical properties were studied using Versatat 4-500 electrochemical workstation (Princeton Applied Research, USA). A three-electrode system was used for all these measurements: a reference electrode (Hg/HgO), a counter electrode (platinum), and a working electrode (TiNO thin films). The electrolyte solution used was 1M KOH. LSV and CV were performed at a rate of 5 and 50 mV/s, respectively. All EIS measurements were conducted in an applied 10 mV of AC amplitude with the frequency range of 0.05 Hz to 10 kHz. The solution temperature was maintained at 25 ℃ during all electrochemical measurements. In the electrochemical measurements, contact was made from the TiNO side using a metallic crocodile clip and the sample was dipped in the 1 M KOH solution carefully so that the clip did

not touch the solution. The electrical resistivity of the TiNO films is in milli ohm.cm (mΩ.cm) range which is significantly low compared to those of conventional semiconductors. Hence realizing the electrical contacts using metallic crocodile clips is believed not to adversely affect any electrochemical measurements. The area of the sample submerged in the solution was measured carefully to measure the electrochemical current density.

3. Results and Discussion

The XRD diffraction patterns recorded from TiNO thin films grown on single-crystal sapphire substrates in an oxygen pressure of 5, 10, 15, and 25 mTorr are shown in Figure 2. The thickness of these films, measured using cross-sectional scanning electron microscopy and surface profilometry, was 265, 255, 250, and 240 nm, respectively. These thickness values are also in agreement with the film thickness values inferred from the etch rate and time it takes to reach the substrate surface while recording the depth profile in the XPS measurements. The appearance of only a set of parallel planes (111) at 36.7 ° and (222) at 77.4°, suggests that all the films are highly textured. Both (111) and (222) peaks match the JCPDS data of TiNO rock salt structure. The increase in the full width at half maximum (FWHM) of (111) and (222) peaks with increasing oxygen pressure is attributed to a decrease in the average TiNO grain size at higher oxygen pressures.[9] A decrease in the film grain size at higher pressures is thought to be brought about by the enhanced vapor-phase collisions among the evaporated/ablated species. This, in turn, results in reduced adatom mobility on the substrate surface. The decrease in TiNO grain size and consequently, the increase in the grain boundary density is manifested in the rise in electrical resistivity, as presented in the next section. A careful examination of the XRD patterns has shown that with an increase in oxygen pressure, the positions of both (111) and (222) peaks shifts rightward with respect to pure TiN film peak positions, marked by two red lines on the x-axis. From the d-values of these peaks, lattice constants of the TiNO films were calculated as a function of oxygen pressures employed during growth, which is plotted in the inset of Figure 2.

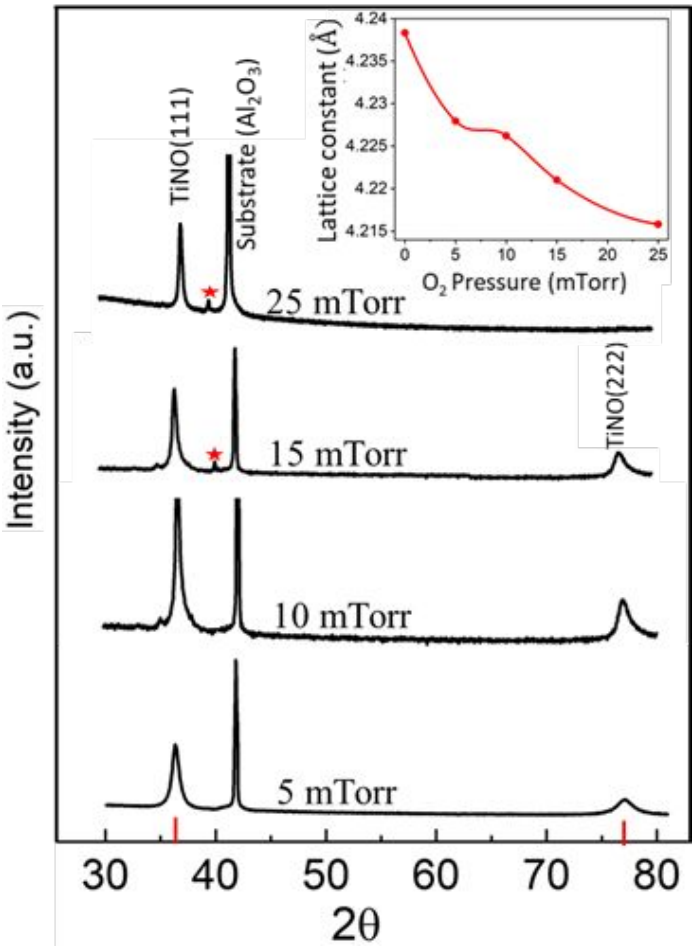

Figure 2. X-ray diffraction patterns of TiNO thin films grown at different oxygen pressure.

As a reference, we have also plotted the lattice constant of a pure TiN film, which was grown in a vacuum of 1.6 $\times 10^{-7}$ Torr with no intentional bleeding of oxygen to the growth chamber. The lattice constant of the pure TiN film (0.424 nm), determined using the XRD d-values, matches well to the theoretical lattice constant of TiN (0.426 nm) calculated using the ionic radii of Ti^{3+} (0.081 nm) and N^{3-} (0.132 nm) and rock salt model of TiN lattice. The increase in the TiNO lattice constants progressively with an increase in the oxygen growth pressure (inset, Figure 2) is attributed to substitution of more N by O, which has smaller ionic radii (0.100 nm) with respect to that of N (0.132 nm). A minor peak corresponding to rutile TiO_2 has also been noticed at 41.2°, as marked by * in the diffraction patterns for TiNO films grown in oxygen pressures above 15 mTorr. The XPS results also confirm the trace presence

of TiO_2 phase in TiNO film grown in higher oxygen pressures; however, the predominant phase remains TiNO in all the oxygen pressure range employed in the present study.[27, 28] The SEM images of the surface morphology of TiNO films are displayed in Fig. 3. All the images were recorded using the same magnification. It is clear from these images that all the films are smooth and are free from any particulate at this magnification. The TiNO grain size was found to be 100, 95, 80, and 65 nm in the TiNO films grown in 5, 10, 15, and 25 mTorr oxygen, respectively. The SEM grain size error was in the range of ±5 nm. The inverse dependence of the grain size on the oxygen pressure used during the film growth is attributed to higher gas phase inelastic collisions of the ablated species. The enhanced gas phase inelastic collisions result in lowering of the velocities of the forward moving ablated species that is manifested in the reduced surface mobility of the ablated species eventually arriving at the substrate surface, and hence, in the reduction in the net TiNO grain size.

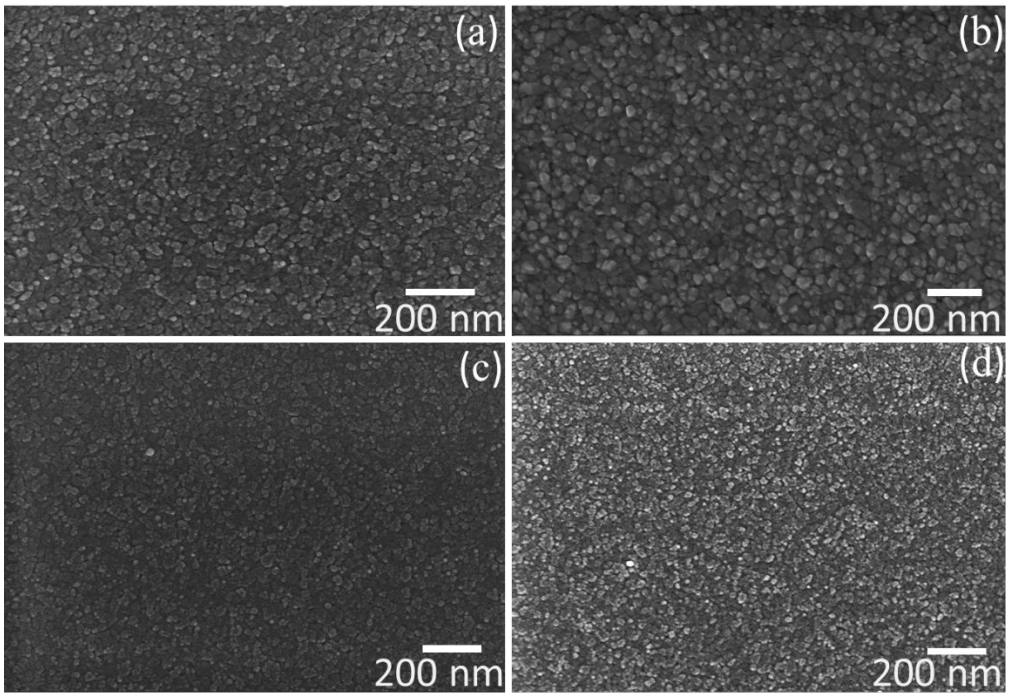

Figure 3. SEM images of TiNO films grown in oxygen pressures of (a) 5 mTorr, (b) 10 mTorr, (c) 15 mTorr, and (d) 25 mTorr.

The XPS spectra of Ti_{2p}, $O_{1s,}$ and N_{1s} recorded from the sputter clean TiNO samples are presented in Figure 4. The TiNO films were surface cleaned for 15 seconds by Argon (Ar) ion etching to remove carbon, nitrogen, and oxygen adsorbed on the film surface from the ambient after TiNO depositions.[51] As seen in Figure 4a, the Ti_{2p} spectrum consists of three distinct peaks. The $Ti2p_{3/2}$ peak (labeled P3) around 455 eV is associated with the Ti-N bonding in TiN. The peak, labeled P2, around 457 eV is associated with oxynitride (Ti-O-N). The peak (labeled P1) around 460 eV refers to the oxide component in TiO_2. The labeling of these peaks is based on the standard XPS peak parameters used for the evaluation of pure TiN and oxidized TiN samples.[9, 51-54] TiN ($Ti_{2p3/2}$ - 455.2 eV), Ti-N-O ($Ti_{2p3/2}$ - 457.4 eV), O^{2-} (O_{1s} - 530.1 eV), and N^{3-} (N_{1s} - 397.2 eV). The intensity profile of these peaks indicates an overall decrease in P1 intensity coupled with an overall decrease in the intensity of P2 and P3 with increasing oxygen partial pressure used during the film deposition. The shift in the peak position from 530.78 eV to 530.48 eV for O1s (Figure 4b), and from 396.58eV to 396.48 eV for N1s (Figure 3c) with an increase in oxygen pressure from 5 to 25 mTorr also lends credence to the increased level of oxidation of TiNO films. The XPS compositions of the TiNO film deposited in 5, 10, 15, and 25 mTorr oxygen pressures were found to be $TiN_{0.57}O_{0.76}$, $TiN_{0.44}O_{0.99}$, $TiN_{0.37}O_{1.19}$, and $TiN_{0.29}O_{1.25}$ after 15 s of Ar-ions surface etch. The variation in the XPS elemental composition in the TiNO films due to a change in oxygen pressure is very informative in the calculation of substitutional point defects in TiNO films.

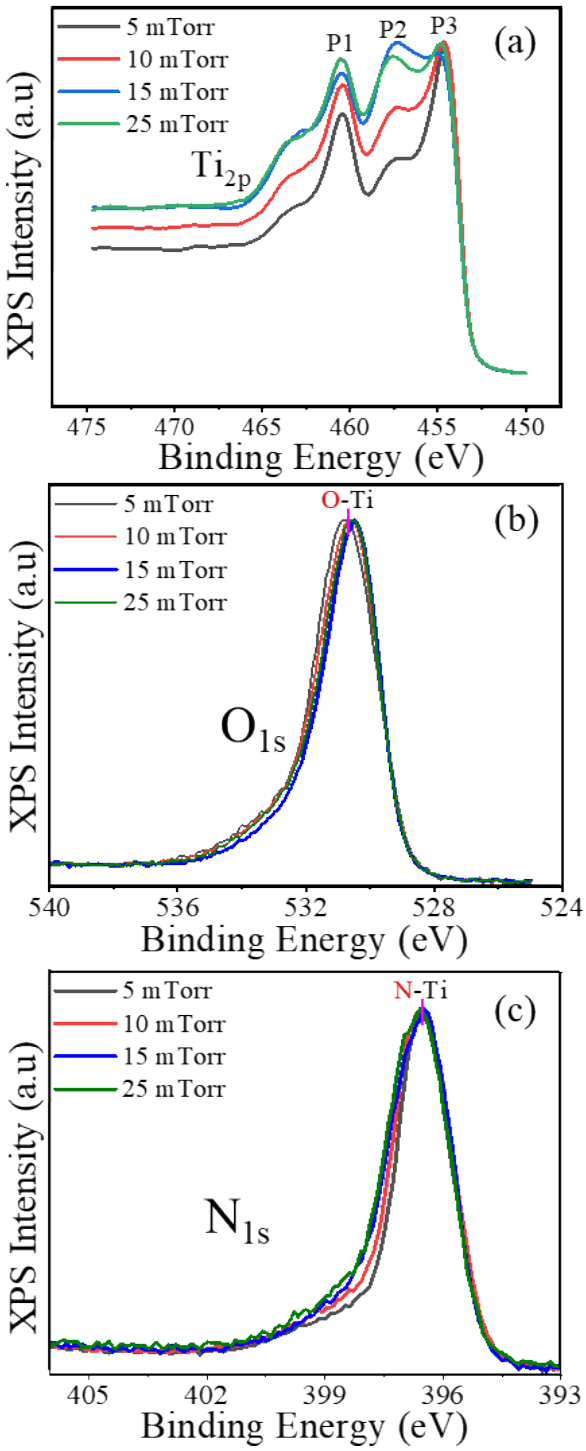

Figure 4. XPS spectra of (a) Ti2p, (b) O1s, and (c) N1s recorded from sputtered clean TiNO films grown at different oxygen pressures.

The variation of electrical resistivity of TiNO films, grown in different oxygen pressures keeping other deposition parameters constant, was studied as a function of temperature using a standard four-probe method and gold evaporated contacts. The normalized resistivity of TiNO

thin film samples versus the temperature of measurements is shown in Figure 5. The normalization was carried out with respect to room temperature resistivity of the respective TiNO film to capture the variation of resistivity in one graph as their resistivity differed hugely due to differences in the oxygen growth pressures. The normalized resistivity values for all the films appear to be zero at 300 K in Figure 5. However, the actual values of 300 K resistivity are 6, 19, 36, and 69 mΩ.cm for TiNO films deposited in 5, 10, 15, and 25 mTorr oxygen pressure, respectively. The values of resistivity of these films at 200, 100 K, and 10 K are listed in Table 1. The decrease in resistivity as temperature increases for all the films is indicative of their electrically semiconducting behavior. Shown, for comparison, is the resistivity plot for a TiN film grown under identical conditions but in high vacuum (2×10^{-7} Torr) with no external gas. The metallic characteristic (increase in resistivity as temperature increases) of a pure TiN film grown in a high vacuum condition is well reported.[10]

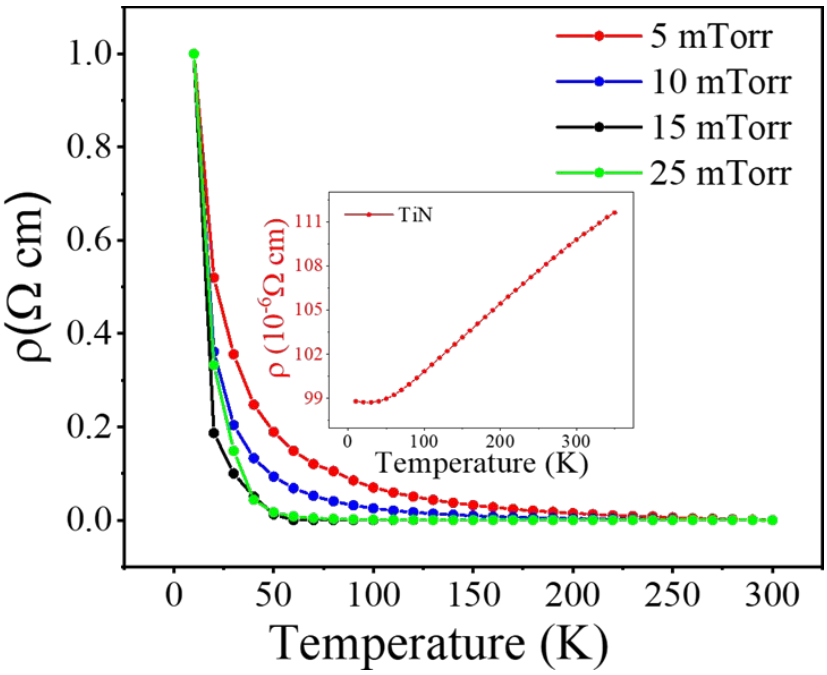

Figure 5. Normalized resistivity of TiNO thin films at various oxygen pressures with respect to temperature (inset) resistivity of pure TiN thin films.

Table 1: Resistivity data of TiNO films at different temperatures.

Oxygen Pressure	300K (mΩ.cm)	200K (mΩ.cm)	100K (mΩ.cm)	10K (mΩ.cm)
5 mTorr	6.4	12.3	34.3	408.0
10 mTorr	19.2	30.1	126.9	4481.0
15 mTorr	36.3	80.1	189.0	2504500.0
25 mTorr	69.3	313.9	5308.8	5383020.0

The conversion of metallic TiN to semiconducting TiNO films via oxygen doping is explained using a simple band diagram shown in Figure 6. The diagram shows that when N atoms in TiN are substituted by O atoms, the top edge of the valence band (VB) moves progressively up with respect to the valence band maximum edge position in the pure TiO_2. The position of the conduction band (CB) minimum due to Ti(3d) remains unaffected in the process of alteration taking place at the anion sites. The upward shift of the VB maximum in the oxynitride system with respect to the VB position in pure TiO_2 can be understood by considering the fact that the VB in the oxynitride is the hybrid of O(2p) and N(2p) orbitals. This bandgap engineering can also be looked at in an alternative manner.[19, 55, 56] The metallic characteristics of pure TiN are well explained due to an overlapping N(2p) VB and Ti(3d) CB, as represented in the central upper part of Figure 6. A substitution of N by O can lead to creating a gap between VB and CB that keeps increasing continually until the TiN phase is transformed to fully to an insulating TiO_2 phase with a bandgap of more than 3.0 eV; also shown in the band diagram the water oxidation and reduction potential (V) with respect to a normal hydrogen electrode (NHE). As illustrated in the right part of Figure 6, if the redox potential of an electrolyte is aligned well to either VB or CB, the water oxidation or reduction kinetics will be fast.[29, 57, 58]

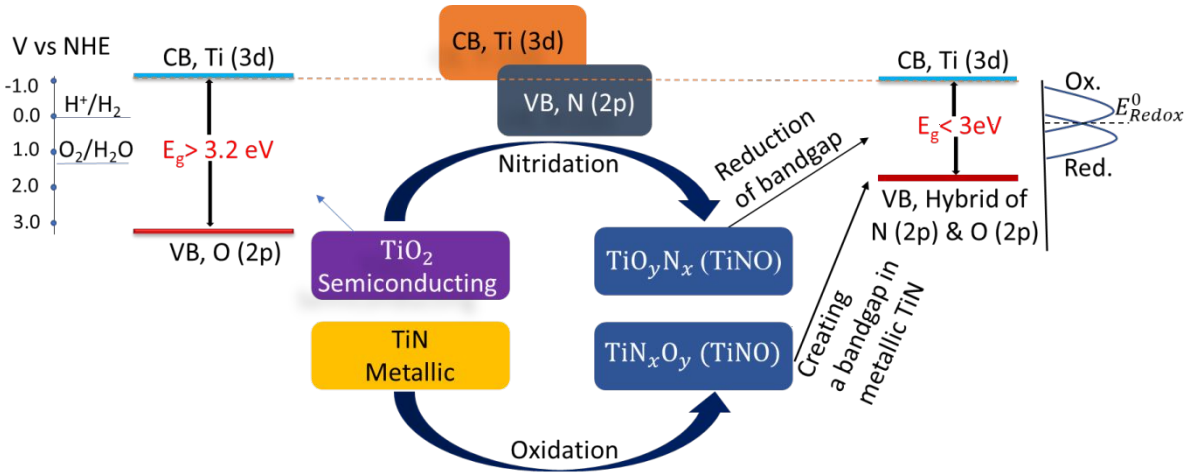

Figure 6. Band diagram showing a downward movement of VB via nitridation of TiO_2 and opening of a bandgap between overlapping valence and conduction band in a metallic TiN via oxidation of TiN.

The electrochemical performance of TiNO samples as efficient OER electrocatalyst has been investigated using linear sweep voltammetry (LSV) in 1M KOH. The results obtained are shown in Figure 7(a), where the current density is plotted as a function of sweeping potential for four samples that were made in oxygen pressures of 5 mTorr to 25 mTorr. Applying the standard 10 mA/cm^2 current density criterion, the overpotential of TiNO thin films deposited in 5, 10, 15, and 25 mTorr oxygen pressure are found to be 340, 320, 310, and 290 mV, respectively. The current density of 10 mA/cm^2 criterion is universally accepted because a device with 10% solar-to-hydrogen conversion efficiency produces this current density under 1-sun illumination.[34] A comparison of the overpotential values realized in the TiNO films with the reported values of OER overpotential in the recent workplaces the TiNO system among the well-established water oxidation catalysts in alkaline media. To name a few other examples metal alloys, nitrides, and oxides such as FeCoNi (291 mV),[17] Co_2N (413 mV), Ni_3N (388 mV), FeCo (371 mV),[17] CoNi (366 mV), FeNi (350 mV),[17] Ir-C, RuO_2, and IrO_2,[17] NiFe-LDH single-layer nanosheets (302 mV),[59] monolayer NiV-LDH (318 mV),[60] $NiCo_2O_4$ ultrathin nanosheets (320 mV), [61] CoMnP nanoparticles (330 mV),[62] $Co_3O_4/NiCo_2O_4$ double-shelled nanocages (340

mV),[63] single crystal Co_3O_4@CoO (430 mV),[64] O-NiCoFe-LDH (420 mV),[65] and Ni-Co mixed oxide cages (380 mV).[66]

The kinetics of the OER of these films have been analyzed using Tafel slopes. The Tafel slopes are shown in Figure 7(b) that is obtained by plotting potential versus the log of the current density. The Tafel slopes are calculated to be 85, 74, 70, and 57 mV/decade for the TiNO films grown in 5, 10, 15, and 25 mTorr oxygen, respectively. These results also demonstrate the advantage of TiNO thin film catalysts. The Tafel slopes for TiNO films grown in 15 and 25 mTorr oxygen are lower than those in FeCoNi (63.8 mV/decade),[17] IrO_2 (87.3 mV), RuO_2 (136.1 mV/decade, and Pt/C (174.7 mV/decade), revealing its superior reaction kinetics.[17, 27, 67] The Nyquist plots obtained from the electrochemical impedance spectroscopy (EIS) measurements at 1.55 vs RHE are shown in Figure 7 (c). A simplified equivalent electrical circuit (EEC), shown in Figure 8, can be used to explain these EIS data. In the EEC, the electrochemical impedance spectra are represented as combinations of circuit elements such as resistors and capacitors. In this circuit, R_1 is the electrolyte resistance, R_2 is the charge transfer resistance at the interface (electrical double layer) between electrolyte and TiNO electrode and, R_3 is the resistance of the TiNO coating layer.[68-70] C is the capacitance of the interfacial layer. The circuit shows that R_1 and R_3 are connected in series with R_2 and C. R_2 and C are themselves connected in parallel as indicated by the dotted circle in Figure 8. The equivalent impedance/resistance of the circuit is given by

$$Z_{eq} = R_1 + \left(\frac{1}{\frac{1}{R_2} + \frac{1}{Z_C}}\right) + R_3 = R_1 + R_3 + \left(\frac{R_2}{1 + R_2 j\omega C}\right), \quad (1)$$

where Z_c is the capacitance of the impedance, j = $\sqrt{-1}$, and ω is the angular frequency. The Nyquist plot arises from the electrical circuit contained in the dotted circle of Figure 7. The semicircle is characteristic of a single time constant and its diameter (Z' in Figure 6 c) represents the charge transfer resistance (R_2). Smaller is the diameter, smaller is the charge transfer

resistance, and hence faster is the reaction kinetics.[71-76] Thus, as seen in the Nyquist plots in Figure 7 (c), the TiNO film grown in 25 mTorr oxygen has the smallest diameter among all the films indicating the least charge transfer resistance, and hence, the best electrochemical catalytic behavior.[72, 74, 77] It should be noted that the diameter of the Nyquist plot is not affected by the contact resistance of electrode materials since the diameter of the Nyquist plot is calculated from the difference of the high and low-frequency x-axis data.

The improvement in the electrocatalytic behavior of TiNO thin films is explained based on proliferation in the number of active sites on the electrode surface by means of substitutional defects in the lattice.[4, 78] As was seen in Figure 1, oxygen can substitute nitrogen positions fully or partially in the TiN rock-salt lattice. Each substitutional site, a point defect in the lattice, serves as an active site for the OER reaction with an enhanced reaction rate. Using the XPS compositions described earlier ($TiN_{0.57}O_{0.76}$, $TiN_{0.44}O_{0.99}$, $TiN_{0.37}O_{1.19}$, and $TiN_{0.29}O_{1.25}$ films grown in 5, 10, 15, and 25 mTorr, respectively), the volume substitutional point defect densities in these films are calculated to be $2.2\times10^{22}/cm^3$, $2.9\times10^{22}/cm^3$, $3.4\times10^{22}/cm^3$, and $3.8\times10^{22}/cm^3$, respectively. The calculation of the volume substitutional point defect density is based on the maintenance of charge neutrality in the lattice and the protection of TiNO's rock salt structure. To preserve these two conditions, oxygen in excess to the N and O stoichiometry additive value of unity leaves the lattice. The excess oxygen combines with Ti, which is also forced to leave the lattice to maintain the charge neutrality that comes in effect due to the substitution of trivalent N ions with bivalent oxygen ions. To illustrate this point, let's take the last sample with $TiN_{0.29}O_{1.25}$ composition. This composition could be alternatively be written as $TiN_{0.29}O_{0.71+0.54}$. The first subscript number (0.71) on O stands for the fractional level of N substitution, while the second subscript number (0.54) on O stands for excess oxygen. Now, to maintain the charge neutrality in the lattice, 0.29 Ti ion per formula unit should leave the lattice, creating Ti cation vacancies in the lattice. Subsequently, 0.29 Ti, and the excess 0.54 O is

believed to combine to form an almost stoichiometric titanium oxide, $Ti_{0.29}O_{0.54}$ ($\equiv TiO_{1.9}$). It may be recalled that both XRD and XPS measurements have indeed shown the presence of TiO_2, especially for samples deposited in higher oxygen pressures. The surface densities of the substitution defects or equivalently the surface-active sites on the TiNO film surfaces, grown in 5, 10, 15, and 25 mTorr, are calculated by multiplying the volume density by film's thickness assuming a uniform distribution of defects in the films' body. These values are found to be $5.8\times10^{17}/cm^2$ $7.4\times10^{17}/cm^2$, $8.5\times10^{17}/cm^2$, and $9.1\times10^{17}/cm^2$, respectively. Even if this calculation gives an approximate estimation of the surface density, a proportionality between volume defect density and surface defect density is well accepted. Thus, we have seen that TiNO film grown in 25 mTorr has the highest substitutional defects density among our samples, which results in the realization of the smallest OER overpotential and the fastest reaction kinetics.[4, 78] Finally, the electrochemical stability of TiNO films has been tested by recording the current density as a function of time in the same electrolytic solution at an applied voltage of 1.55 V versus RHE. The results obtained are shown for all the four TiNO samples in Figure 9, which show that the current density decays almost negligibly for all the samples for 12 hours. Though the time of this study is short, it demonstrates their stable electrochemical behavior which is critical for their practical application.[79]

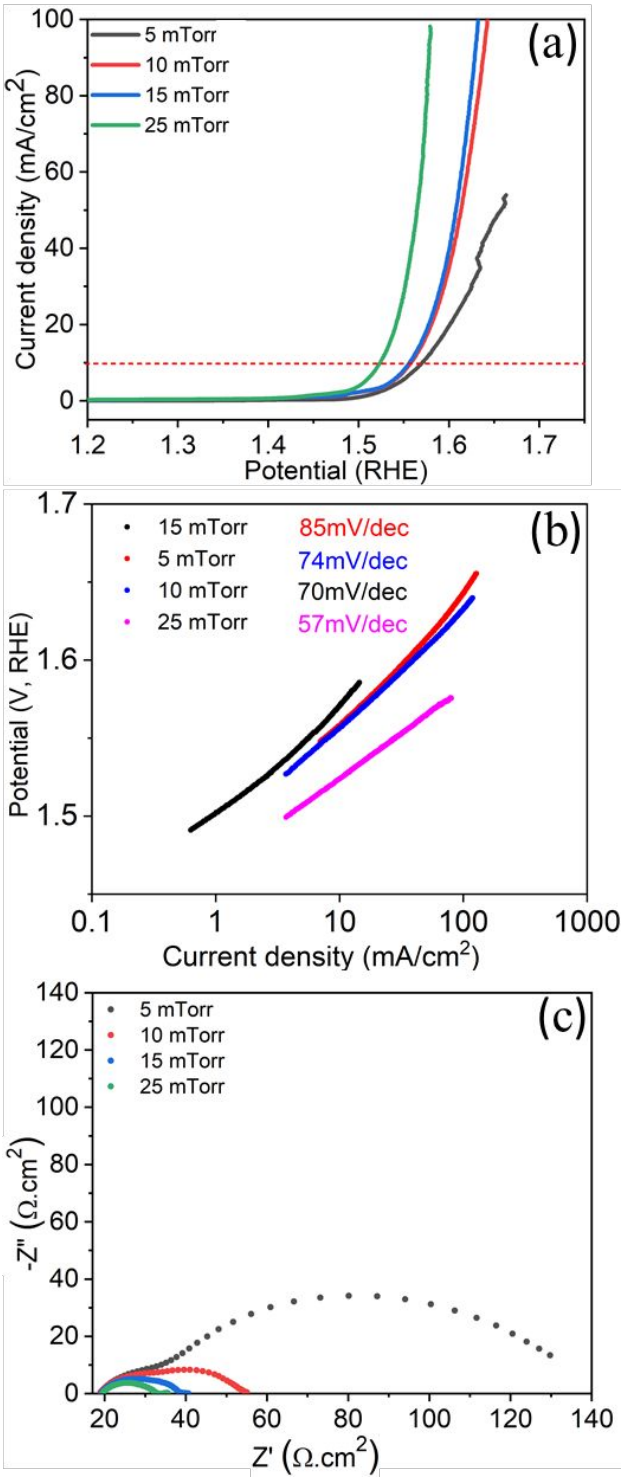

Figure 7. (a) Polarization curves (b) Tafel plots, and (c) Nyquist plots for TiN thin films grown in 5, 10, 15, and 25 m Torr of oxygen pressure.

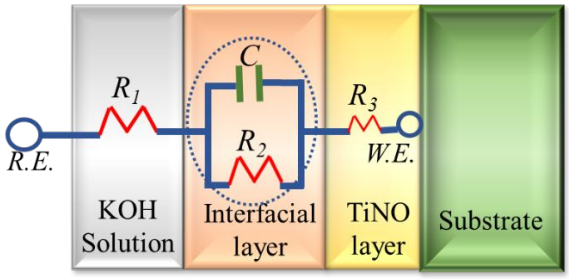

Figure 8. Schematic representation of an equivalent electrical circuit used to explain Nyquist plots. Please note that image is not to the scale; for example, the dimension of interfacial and TiNO layers are several orders of magnitude smaller than that of the substrate. R.E. is the reference electrode and W.E. is the working electrode.

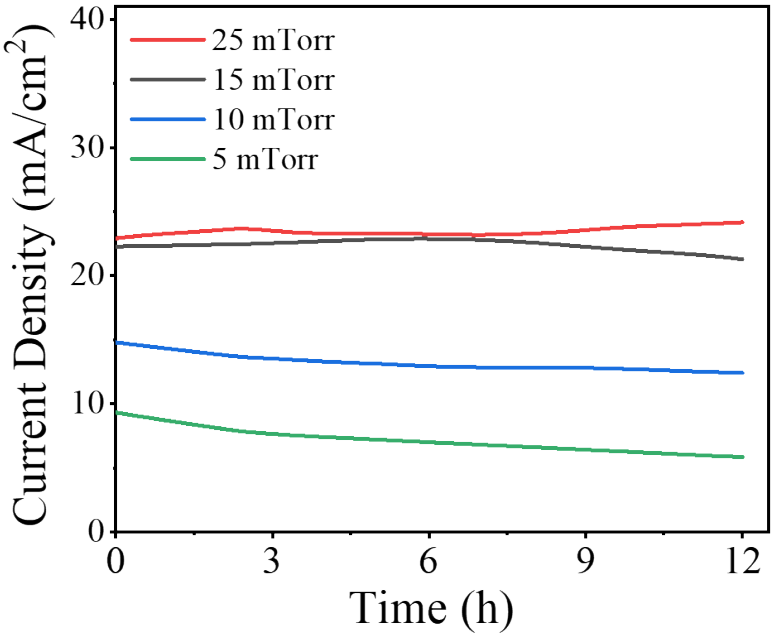

Figure 9. Time-dependent current density plots for TiNO films at 1.55 V vs RHE for 12 h.

4. Conclusions

In summary, a pulsed laser deposition method has been used to synthesize semiconducting thin film TiO_xN_y compounds with varying x and y by simply changing the oxygen pressure during the film growth. The overpotential for oxygen evolution reaction realized for these films is in the range of 320 -290 mV, which are amongst the lowest values reported for any oxynitride systems to date. The Tafel slopes for these films are determined to be in the rage of 57-85 mv/decade. The improvement in the electrocatalytic behavior of TiNO thin films in terms of reduced OER overpotential and fast reaction kinetic is explained on the

basis of an enhanced number of electrochemically active sites realized by the substitution of anionic N sites by O and a favorable alignment of valence band with respect to the redox potential of electrolyte medium. These findings appear to assume significant importance in light of water electrolysis to produce fossil-free fuels for the development of environmentally friendly power sources.

AUTHOR INFORMATION

Corresponding Author

Dhananjay Kumar – Department of Mechanical Engineering, North Carolina Agricultural and Technical State University, Greensboro, NC 27455; Phone: 336-285-3227; Email: dkumar@ncat.edu

Authors

Nikhil Reddy Mucha – Department of Mechanical Engineering, North Carolina Agricultural and Technical State University, Greensboro, NC 27455; Email: nmucha@aggies.ncat.edu

Jacob Som – Department of Mechanical Engineering, North Carolina Agricultural and Technical State University, Greensboro, NC-27455; Email: jsom@aggies.ncat.edu

Jonghyun Choi – Department of Chemistry, Pittsburg State University, 1701 South Broadway Street, Pittsburg, KS 66762; Email: jonghyun.choi@gus.pittstate.edu

Surabhi Shaji – Department of Mechanical Engineering, North Carolina Agricultural and Technical State University, Greensboro, NC-27455; Email: sshaji@aggies.ncat.edu

Rama Krishna Gupta – Department of Chemistry, Pittsburg State University, 1701 South Broadway Street, Pittsburg, KS 66762; Email: rgupta@pittstate.edu

Harry M. Meyer – Center for Nanophase Materials Sciences, Oakridge National Laboratory, Oakridge, TN-37831; Email: meyerhmiii@ornl.gov

Corson L. Cramer – Energy and Transportation Sciences Division, Oakridge National Laboratory, Oakridge, TN-37831; Email: cramercl@ornl.gov

Amy M. Elliot – Energy and Transportation Sciences Division, Oakridge National Laboratory, Oakridge, TN-37831; Email: elliottam@ornl.gov

Notes

The authors declare no competing financial interest.

Acknowledgements

DK would like to acknowledge the financial support from the National Science Foundation (NSF) through the Nebraska Materials Research Science and Engineering Center (MRSEC) Grant. No. DMR-1420645 and the University of North Carolina (UNC) system for the seed funding via Interinstitutional Planning Grant (IPG). The graduate students, Nikhil Mucha, Jacob Som, and Surabhi Shaji, were supported from the DMR-1420645 grant.

References

1. Fujishima, A.; Honda, K., Electrochemical Photolysis of Water at a Semiconductor Electrode. *Nature* **1972,** *238*, 37.
2. Brancho, J. J.; Bartlett, B. M., Challenges in Co-Alloyed Titanium Oxynitrides, a Promising Class of Photochemically Active Materials. *Chemistry of Materials* **2015,** *27* (21), 7207-7217.
3. Gebauer, C.; Fischer, P.; Wassner, M.; Diemant, T.; Jusys, Z.; Hüsing, N.; Behm, R. J., Performance of titanium oxynitrides in the electrocatalytic oxygen evolution reaction. *Nano Energy* **2016,** *29*, 136-148.
4. Kuraganti, V.; Jain, A.; Bar-Ziv, R.; Ramasubramaniam, A.; Bar-Sadan, M., Manganese doping of MoSe2 promotes active defect sites for hydrogen evolution. *ACS applied materials & interfaces* **2019,** *11* (28), 25155-25162.
5. Sinhamahapatra, A.; Jeon, J.-P.; Yu, J.-S., A new approach to prepare highly active and stable black titania for visible light-assisted hydrogen production. *Energy & Environmental Science* **2015,** *8* (12), 3539-3544.
6. Yang, J. Y.; Bullock, R. M.; DuBois, M. R.; DuBois, D. L., Fast and efficient molecular electrocatalysts for H2 production: Using hydrogenase enzymes as guides. *MRS Bulletin* **2011,** *36* (1), 39-47.
7. Zou, X.; Zhang, Y., Noble metal-free hydrogen evolution catalysts for water splitting. *Chemical Society Reviews* **2015,** *44* (15), 5148-5180.
8. Kumar, D.; Oh, S. H.; Pennycook, S. J.; Majumdar, A. K., Scaling exponent within the side-jump mechanism of Hall effect size-dependence in Ni nanocrystals. *Applied Physics Letters* **2008,** *93* (13), 133105.
9. Mucha, N. R.; Som, J.; Shaji, S.; Fialkova, S.; Apte, P. R.; Balasubramanian, B.; Shield, J. E.; Anderson, M.; Kumar, D., Electrical and optical properties of titanium oxynitride thin films. *Journal of Materials Science* **2020,** *55* (12), 5123-5134.
10. Roy, M.; Mucha, N. R.; Ponnam, R. G.; Jaipan, P.; Scott-Emuakpor, O.; Yarmolenko, S.; Majumdar, A. K.; Kumar, D., Quantum interference effects in titanium nitride films at low temperatures. *Thin Solid Films* **2019,** *681*, 1-5.
11. Jaipan, P.; Nannuri, C.; Mucha, N. R.; Singh, M. P.; Xu, Z.; Moatti, A.; Narayan, J.; Fialkova, S.; Kotoka, R.; Yarmolenko, S.; Scott-Emuakpor, O.; Binek, C.; Kebede, A.; Kumar, D., Influence of Gold Catalyst on the Growth of Titanium Nitride Nanowires. *Jaipan, Panupong* **2018,** *7* (5), 720-725(6).
12. Narayan, J.; Biunno, N.; Singh, R.; Holland, O.; Auciello, O., Formation of thin superconducting films by the laser processing method. *Applied physics letters* **1987,** *51* (22), 1845-1847.
13. Rasic, D.; Sachan, R.; Chisholm, M. F.; Prater, J.; Narayan, J., Room Temperature Growth of Epitaxial Titanium Nitride Films by Pulsed Laser Deposition. *Crystal Growth & Design* **2017,** *17* (12), 6634-6640.
14. Faruque, M. K.; M-Darkwa, K.; Xu, Z.; Kumar, D., Fabrication, characterization, and mechanism of vertically aligned titanium nitride nanowires. *Applied Surface Science* **2012,** *260*, 36-41.
15. Gbordzoe, S.; Kotoka, R.; Craven, E.; Kumar, D.; Wu, F.; Narayan, J., Effect of substrate temperature on the microstructural properties of titanium nitride nanowires grown by pulsed laser deposition. *Journal of Applied Physics* **2014,** *116* (6), 064310.
16. Sarkar, K.; Jaipan, P.; Choi, J.; Haywood, T.; Tran, D.; Mucha, N. R.; Yarmolenko, S.; Scott-Emuakpor, O.; Sundaresan, M.; Gupta, R. K., Enhancement in corrosion resistance and vibration damping performance in titanium by titanium nitride coating. *SN Applied Sciences* **2020,** *2*, 1-14.

17. Di, J.; Zhu, H.; Xia, J.; Bao, J.; Zhang, P.; Yang, S.-Z.; Li, H.; Dai, S., High-performance electrolytic oxygen evolution with a seamless armor core–shell FeCoNi oxynitride. *Nanoscale* **2019,** *11* (15), 7239-7246.
18. Jia, L.; Lu, H.; Ran, Y.; Zhao, S.; Liu, H.; Li, Y.; Jiang, Z.; Wang, Z., Structural and dielectric properties of ion beam deposited titanium oxynitride thin films. *Journal of Materials Science* **2019,** *54* (2), 1452-1461.
19. Maeda, K.; Domen, K., Oxynitride materials for solar water splitting. *MRS Bulletin* **2011,** *36* (1), 25-31.
20. Rawal, S. K.; Chawla, A. K.; Chawla, V.; Jayaganthan, R.; Chandra, R., Effect of ambient gas on structural and optical properties of titanium oxynitride films. *Applied Surface Science* **2010,** *256* (13), 4129-4135.
21. Sowińska, M.; Brizzi, S.; Das, C.; Kärkkänen, I.; Schneidewind, J.; Naumann, F.; Gargouri, H.; Henkel, K.; Schmeißer, D., Analysis of nitrogen species in titanium oxynitride ALD films. *Applied Surface Science* **2016,** *381*, 42-47.
22. Yoo, J. B.; Yoo, H. J.; Jung, H. J.; Kim, H. S.; Bang, S.; Choi, J.; Suh, H.; Lee, J.-H.; Kim, J.-G.; Hur, N. H., Titanium oxynitride microspheres with the rock-salt structure for use as visible-light photocatalysts. *Journal of Materials Chemistry A* **2016,** *4* (3), 869-876.
23. Shi, X.; Xu, L.; Le, T. B.; Zhou, G.; Zheng, C.; Tsuru, K.; Ishikawa, K., Partial oxidation of TiN coating by hydrothermal treatment and ozone treatment to improve its osteoconductivity. *Materials Science and Engineering: C* **2016,** *59*, 542-548.
24. Shin, P.-K.; Mikolajick, T., Alkali- and hydrogen ion sensing properties of LPCVD silicon oxynitride thin films. *Thin Solid Films* **2003,** *426* (1), 232-237.
25. Takeshi, M.; Ryoji, A.; Takeshi, O.; Koyu, A.; Yasunori, T., Band-Gap Narrowing of Titanium Dioxide by Nitrogen Doping. *Japanese Journal of Applied Physics* **2001,** *40* (6A), L561.
26. Tompkins, H. G., The initial stages of the oxidation of titanium nitride. *Journal of Applied Physics* **1992,** *71* (2), 980-983.
27. Wang, W.; Savadogo, O.; Ma, Z.-F., Preparation of new titanium oxy nitride based electro catalysts using an anhydrous sol-gel method for water electrolysis in acid medium. *International Journal of Hydrogen Energy* **2012,** *37* (9), 7405-7417.
28. Wu, Z.; Dong, F.; Zhao, W.; Guo, S., Visible light induced electron transfer process over nitrogen doped TiO2 nanocrystals prepared by oxidation of titanium nitride. *Journal of Hazardous Materials* **2008,** *157* (1), 57-63.
29. Zhang, J. Z., Metal oxide nanomaterials for solar hydrogen generation from photoelectrochemical water splitting. *MRS Bulletin* **2011,** *36* (1), 48-55.
30. Graciani, J.; Hamad, S.; Sanz, J. F., Changing the physical and chemical properties of titanium oxynitrides TiN 1− x O x by changing the composition. *Physical Review B* **2009,** *80* (18), 184112.
31. McKenna, K. P., Structure, electronic properties, and oxygen incorporation/diffusion characteristics of the Σ 5 TiN(310)[001] tilt grain boundary. *Journal of Applied Physics* **2018,** *123* (7), 075301.
32. Haydous, F.; Döbeli, M.; Si, W.; Waag, F.; Li, F.; Pomjakushina, E.; Wokaun, A.; Gökce, B.; Pergolesi, D.; Lippert, T., Oxynitride Thin Films versus Particle-Based Photoanodes: A Comparative Study for Photoelectrochemical Solar Water Splitting. *ACS Applied Energy Materials* **2019,** *2* (1), 754-763.
33. Chang, S. H.; Danilovic, N.; Chang, K.-C.; Subbaraman, R.; Paulikas, A. P.; Fong, D. D.; Highland, M. J.; Baldo, P. M.; Stamenkovic, V. R.; Freeland, J. W., Functional links between stability and reactivity of strontium ruthenate single crystals during oxygen evolution. *Nature communications* **2014,** *5* (1), 1-9.

34. Seitz, L. C.; Dickens, C. F.; Nishio, K.; Hikita, Y.; Montoya, J.; Doyle, A.; Kirk, C.; Vojvodic, A.; Hwang, H. Y.; Norskov, J. K., A highly active and stable IrOx/SrIrO3 catalyst for the oxygen evolution reaction. *Science* **2016,** *353* (6303), 1011-1014.
35. Seh, Z. W.; Kibsgaard, J.; Dickens, C. F.; Chorkendorff, I.; Nørskov, J. K.; Jaramillo, T. F., Combining theory and experiment in electrocatalysis: Insights into materials design. *Science* **2017,** *355* (6321), eaad4998.
36. Benck, J. D.; Hellstern, T. R.; Kibsgaard, J.; Chakthranont, P.; Jaramillo, T. F., Catalyzing the Hydrogen Evolution Reaction (HER) with Molybdenum Sulfide Nanomaterials. *ACS Catalysis* **2014,** *4* (11), 3957-3971.
37. Benck, J. D.; Chen, Z.; Kuritzky, L. Y.; Forman, A. J.; Jaramillo, T. F., Amorphous Molybdenum Sulfide Catalysts for Electrochemical Hydrogen Production: Insights into the Origin of their Catalytic Activity. *ACS Catalysis* **2012,** *2* (9), 1916-1923.
38. Kortlever, R.; Shen, J.; Schouten, K. J. P.; Calle-Vallejo, F.; Koper, M. T. M., Catalysts and Reaction Pathways for the Electrochemical Reduction of Carbon Dioxide. *The Journal of Physical Chemistry Letters* **2015,** *6* (20), 4073-4082.
39. Wen, Z.; Cui, S.; Pu, H.; Mao, S.; Yu, K.; Feng, X.; Chen, J., Metal Nitride/Graphene Nanohybrids: General Synthesis and Multifunctional Titanium Nitride/Graphene Electrocatalyst. *Advanced Materials* **2011,** *23* (45), 5445-5450.
40. Avasarala, B.; Haldar, P., Electrochemical oxidation behavior of titanium nitride based electrocatalysts under PEM fuel cell conditions. *Electrochimica Acta* **2010,** *55* (28), 9024-9034.
41. Suhadolnik, L.; Lašič Jurković, D.; Likozar, B.; Bele, M.; Drev, S.; Čeh, M., Structured titanium oxynitride (TiOxNy) nanotube arrays for a continuous electrocatalytic phenol-degradation process: Synthesis, characterization, mechanisms and the chemical reaction micro-kinetics. *Applied Catalysis B: Environmental* **2019,** *257*, 117894.
42. Dutta, S.; Indra, A.; Feng, Y.; Han, H.; Song, T., Promoting electrocatalytic overall water splitting with nanohybrid of transition metal nitride-oxynitride. *Applied Catalysis B: Environmental* **2019,** *241*, 521-527.
43. Chen, X.; Lou, Y.-B.; Samia, A. C. S.; Burda, C.; Gole, J. L., Formation of Oxynitride as the Photocatalytic Enhancing Site in Nitrogen-Doped Titania Nanocatalysts: Comparison to a Commercial Nanopowder. *Advanced Functional Materials* **2005,** *15* (1), 41-49.
44. Chisaka, M.; Ando, Y.; Yamamoto, Y.; Itagaki, N., A Carbon-Support-Free Titanium Oxynitride Catalyst for Proton Exchange Membrane Fuel Cell Cathodes. *Electrochimica Acta* **2016,** *214*, 165-172.
45. Kim, S. Y.; Han, D. H.; Kim, J. N.; Lee, J. J., Titanium oxynitride films for a bipolar plate of polymer electrolyte membrane fuel cell prepared by inductively coupled plasma assisted reactive sputtering. *Journal of Power Sources* **2009,** *193* (2), 570-574.
46. Punugupati, S.; Kumar, R.; Nori, S.; Hunte, F.; Narayan, J., Structural, magnetic and magnetotransport properties of bi-epitaxial La0.7Sr0.3MnO3 (110) thin films integrated on Si (001). *Acta Materialia* **2016,** *106*, 40-47.
47. Kumar, D.; Chattopadhyay, S.; Gilmore, W. M.; Lee, C. B.; Sankar, J.; Kvit, A.; Sharma, A. K.; Narayan, J.; Pietambaram, S. V.; Singh, R. K., Structural and magnetoresistance properties of La2/3Ca1/3MnO3 thin films on buffered silicon substrates. *Applied Physics Letters* **2001,** *78* (8), 1098-1100.
48. Shaji, S.; Mucha, N. R.; Fialkova, S.; Kumar, D., Morphological data on soft ferromagnetic Fe90Ta10 thin films. *Data in Brief* **2019,** *27*, 104714.
49. Shaji, S.; Mucha, N. R.; Majumdar, A.; Binek, C.; Kebede, A.; Kumar, D., Magnetic and electrical properties of Fe90Ta10 thin films. *Journal of Magnetism and Magnetic Materials* **2019,** *489*, 165446.

50. Shaji, S.; Mucha, N. R.; Giri, P.; Binek, C.; Kumar, D., Magnetic and magnetocaloric properties of Fe2Ta thin films. *AIP Advances* **2020,** *10* (2), 025222.
51. Kuznetsov, M. V.; Zhuravlev, J. F.; Zhilyaev, V. A.; Gubanov, V. A., XPS study of the nitrides, oxides and oxynitrides of titanium. *Journal of Electron Spectroscopy and Related Phenomena* **1992,** *58* (1), 1-9.
52. Jaeger, D.; Patscheider, J., Single crystalline oxygen-free titanium nitride by XPS. *Surface Science Spectra* **2013,** *20* (1), 1-8.
53. Kuznetsov, M. V.; Zhuravlev, J. F.; Gubanov, V. A., XPS analysis of adsorption of oxygen molecules on the surface of Ti and TiNx films in vacuum. *Journal of Electron Spectroscopy and Related Phenomena* **1992,** *58* (3), 169-176.
54. Milošv, I.; Strehblow, H. H.; Navinšek, B.; Metikoš-Huković, M., Electrochemical and thermal oxidation of TiN coatings studied by XPS. *Surface and interface analysis* **1995,** *23* (7-8), 529-539.
55. Martin, D. J.; Reardon, P. J. T.; Moniz, S. J.; Tang, J., Visible light-driven pure water splitting by a nature-inspired organic semiconductor-based system. *Journal of the American Chemical Society* **2014,** *136* (36), 12568-12571.
56. Maeda, K.; Domen, K., Photocatalytic Water Splitting: Recent Progress and Future Challenges. *The Journal of Physical Chemistry Letters* **2010,** *1* (18), 2655-2661.
57. Thorne, J. E.; Li, S.; Du, C.; Qin, G.; Wang, D., Energetics at the Surface of Photoelectrodes and Its Influence on the Photoelectrochemical Properties. *The Journal of Physical Chemistry Letters* **2015,** *6* (20), 4083-4088.
58. Kudo, A., Z-scheme photocatalyst systems for water splitting under visible light irradiation. *MRS Bulletin* **2011,** *36* (1), 32-38.
59. Song, F.; Hu, X., Exfoliation of layered double hydroxides for enhanced oxygen evolution catalysis. *Nature communications* **2014,** *5* (1), 1-9.
60. Fan, K.; Chen, H.; Ji, Y.; Huang, H.; Claesson, P. M.; Daniel, Q.; Philippe, B.; Rensmo, H.; Li, F.; Luo, Y., Nickel–vanadium monolayer double hydroxide for efficient electrochemical water oxidation. *Nature communications* **2016,** *7* (1), 1-9.
61. Bao, J.; Zhang, X.; Fan, B.; Zhang, J.; Zhou, M.; Yang, W.; Hu, X.; Wang, H.; Pan, B.; Xie, Y., Ultrathin spinel-structured nanosheets rich in oxygen deficiencies for enhanced electrocatalytic water oxidation. *Angewandte Chemie International Edition* **2015,** *54* (25), 7399-7404.
62. Li, D.; Baydoun, H.; Verani, C. u. N.; Brock, S. L., Efficient water oxidation using CoMnP nanoparticles. *Journal of the American Chemical Society* **2016,** *138* (12), 4006-4009.
63. Hu, H.; Guan, B.; Xia, B.; Lou, X. W., Designed formation of Co3O4/NiCo2O4 double-shelled nanocages with enhanced pseudocapacitive and electrocatalytic properties. *Journal of the American Chemical Society* **2015,** *137* (16), 5590-5595.
64. Tung, C.-W.; Hsu, Y.-Y.; Shen, Y.-P.; Zheng, Y.; Chan, T.-S.; Sheu, H.-S.; Cheng, Y.-C.; Chen, H. M., Reversible adapting layer produces robust single-crystal electrocatalyst for oxygen evolution. *Nature communications* **2015,** *6*, 8106.
65. Qian, L.; Lu, Z.; Xu, T.; Wu, X.; Tian, Y.; Li, Y.; Huo, Z.; Sun, X.; Duan, X., Trinary layered double hydroxides as high-performance bifunctional materials for oxygen electrocatalysis. *Advanced Energy Materials* **2015,** *5* (13), 1500245.
66. Han, L.; Yu, X. Y.; Lou, X. W., Formation of prussian-blue-analog nanocages via a direct etching method and their conversion into ni–co-mixed oxide for enhanced oxygen evolution. *Advanced materials* **2016,** *28* (23), 4601-4605.
67. Mavrokefalos, C. K.; Patzke, G. R., Water Oxidation Catalysts: The Quest for New Oxide-Based Materials. *Inorganics* **2019,** *7* (3), 29.
68. Bard, A. J.; Faulkner, L. R., Fundamentals and applications. *Electrochemical Methods* **2001,** *2* (482), 580-632.

69. Orazem, M. E.; Tribollet, B., *Electrochemical impedance spectroscopy*. John Wiley & Sons: 2017.
70. Wilson, J.; Schwartz, D.; Adler, S. B., Nonlinear electrochemical impedance spectroscopy for solid oxide fuel cell cathode materials. *Electrochimica Acta* **2006,** *51* (8-9), 1389-1402.
71. Akram, R.; Khan, M. D.; Zequine, C.; Zhao, C.; Gupta, R. K.; Akhtar, M.; Akhtar, J.; Malik, M. A.; Revaprasadu, N.; Bhatti, M. H., Cobalt sulfide nanoparticles: Synthesis, water splitting and supercapacitance studies. *Materials Science in Semiconductor Processing* **2020,** *109*, 104925.
72. Ayom, G. E.; Khan, D. M.; Ingsel, T.; Lin, W.; Gupta, R.; Zamisas, S.; Van Zyl, W.; Revaprasadu, N., Flexible Molecular Precursors for Selective Decomposition to Nickel Sulfide or Nickel Phosphide for Water Splitting and Supercapacitance. *Chemistry–A European Journal*.
73. Guragain, D.; Zequine, C.; Poudel, T.; Neupane, D.; Gupta, R.; Mishra, S., Facile Synthesis of Bio-Templated Tubular Co3O4 Microstructure and Its Electrochemical Performance in Aqueous Electrolytes. *Journal of nanoscience and nanotechnology* **2020,** *20* (5), 3182-3194.
74. Zequine, C.; Bhoyate, S.; Wang, F.; Li, X.; Siam, K.; Kahol, P. K.; Gupta, R. K., Effect of solvent for tailoring the nanomorphology of multinary CuCo2S4 for overall water splitting and energy storage. *Journal of Alloys and Compounds* **2019,** *784*, 1-7.
75. Gupta, R. K.; Mensah-Darkwa, K.; Kumar, D., Corrosion Protective Conversion Coatings on Magnesium Disks Using a Hydrothermal Technique. *Journal of Materials Science & Technology* **2014,** *30* (1), 47-53.
76. Mitchell, E.; Gupta, R. K.; Mensah-Darkwa, K.; Kumar, D.; Ramasamy, K.; Gupta, B. K.; Kahol, P., Facile synthesis and morphogenesis of superparamagnetic iron oxide nanoparticles for high-performance supercapacitor applications. *New Journal of Chemistry* **2014,** *38* (9), 4344-4350.
77. Fernández-Ibáñez, P.; de las Nieves, F. J.; Malato, S., Titanium Dioxide/Electrolyte Solution Interface: Electron Transfer Phenomena. *Journal of Colloid and Interface Science* **2000,** *227* (2), 510-516.
78. Zhao, Y.; Balasubramanyam, S.; Sinha, R.; Lavrijsen, R.; Verheijen, M.; Bol, A.; Bieberle-Hütter, A., Physical and chemical defects in WO3 thin films and their impact on photoelectrochemical water splitting. *ACS Applied Energy Materials* **2018,** *1* (11), 5887-5895.
79. Lian, J.; Zhang, F.; Lu, S.; Jiang, W.; Hu, Q.; Li, D.; Zhang, B., Amorphous Fe−Co−P−C Film on a Carbon Fiber Paper Support as an Efficient Electrocatalyst for the Oxygen Evolution Reaction. *Chem Electro Chem* **2019,** *6* (15), 3976-3981.

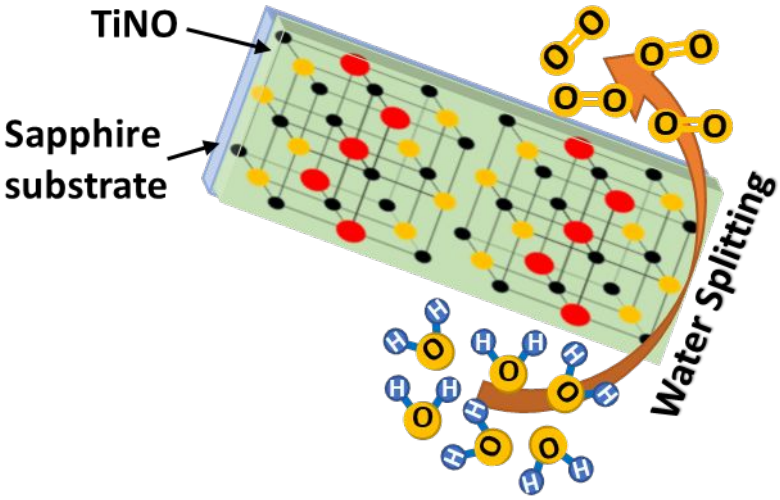

For Table of Content Graphic Only

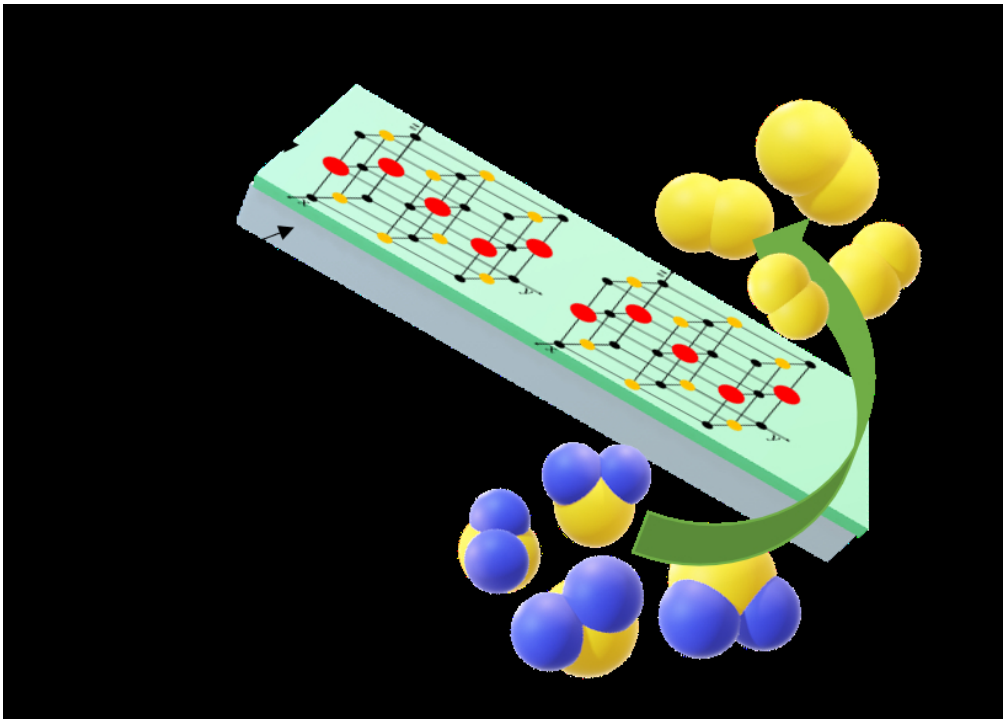

137x98mm (150 x 150 DPI)